Broadband polarization spectrum tuning enabled by the built-in electric field of patterned spintronic terahertz emitters

Qing Yang,[a] Yan Huang,[a] Houyi Cheng,[a, c] Reza Rouzegar,[e] Renyou Xu,[a] Shijie Xu,[a, c] Jie Zhang,[a, b] Fan Zhang,[a, c] Yong Xu,[a, b, c] Lianggong Wen,[a,d] Weisheng Zhao [a, b, c, d] and Tianxiao Nie [a, b, c, d, *]

[a] Beihang University, School of Integrated Circuit Science and Engineering, MIIT Key Laboratory of Spintronics, 37 Xueyuan Road, Beijing, China, 100191

[b] Beihang University, Institute of International Innovation, National Key Lab of Spintronics, No. 99 Changhe Street, Hangzhou, China, 311115

[c] Beihang University, Hefei Innovation Research Institute, 50 meters south of Qianjiang Road, Hefei, China, 230012

[d] Beihang University, Qingdao Innovation Research Institute, No. 393 Songling Road, Qingdao, China, 266000

[e] Freie Universität Berlin, Institute of Physics,16-18 Kaiserswerther Street, Berlin, Germany, 141195

S1 More details of the samples and the process of pattern fabrication

In Fig. S1(a)-(g) show the optical photograph with the aspect ratio 1:1, 1:1.5,1:2,1:10,1:32 and 1:50. Every group remains *l/d* is equal to 5.66. Sketch map of fabricating devices is illustrated in Fig. S1(h), which includes two times of ultraviolet (UV)-lithography, etching and remark the position of patterns via e-beam evaporation.

We used L-edit for designing patterns. During designing, we set each material in different layers and represent them with different colors. Then, we instance each layer into each cell according to the structure of films and achieve the pattern arrangement in the mask.

The fabrication of patterns was based on standard photolithography, etching and e-beam evaporation. After adhesion treatment by O_2, a layer of positive photoresist

(AZ5214, Clariant GmbH) was spun onto the substrate. To reduce the moisture content, the sample was placed on the hot plate (90 ℃) for 90s.The patterns was transferred to the substrates under ultraviolet (UV) exposure of 10s. Inductively coupled plasma etching (PlasmaPro System100/1 ICP180, Oxford) was chosen to remove metal uncovered with photoresist. Finally, Ti (20 nm)/Au (100 nm) was deposited by e-beam evaporation (DZS-500, SKY Technology Development Co., Ltd. Chinese Academy of Sciences). The Au layer is to mark the location of the device. After fabrication, we used optical microscopy and Magneto-optical Kerr effect (MOKE) setup to characterize the morphology and magnetic properties of the devices.

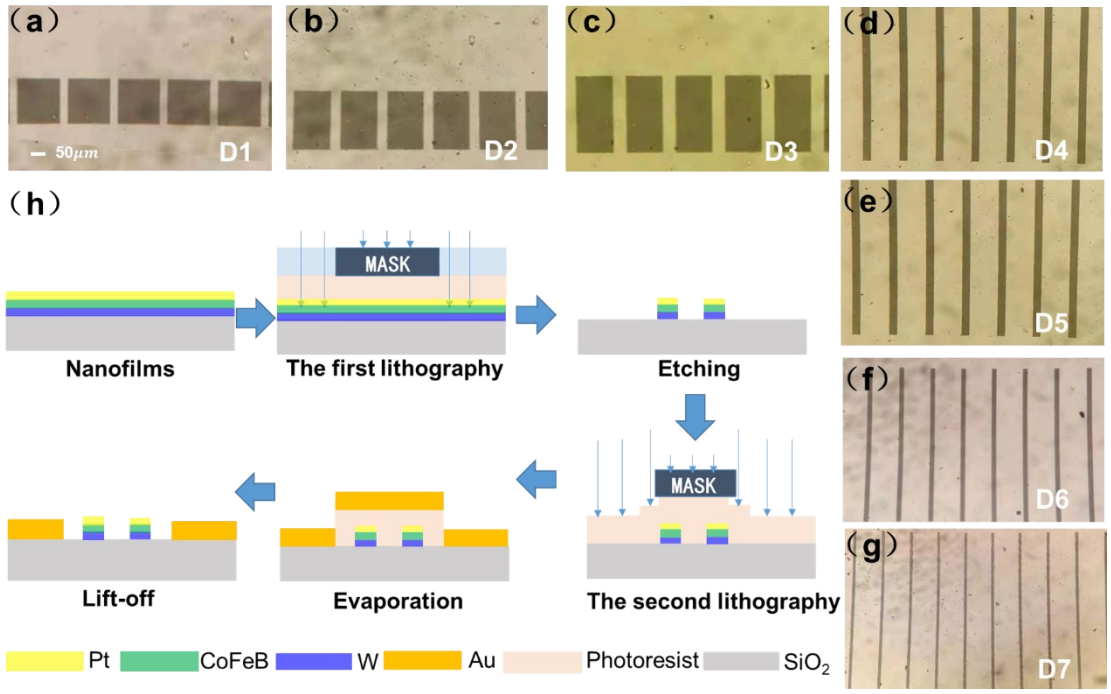

Fig. S1. (a)-(g) Optical photographs of seven groups. **(h)** Fabrication process of the devices.

S2 More details of measurement setup

The terahertz time domain spectroscopy (THz-TDS) system used in our experiment is

driven by a commercial amplified Ti:sapphire laser source delivering a central wavelength of 800nm,a pulse duration of 35 fs and a repetition rate of 1KHz.The laser pulses are divided into two beams where one beam with 90% energy named excitation pulse and the other with 10% energy called probe pulse in Fig. S2.The former with 8mm spot diameter is used to pump the patterned spintronic terahertz emitters for terahertz waves generating, and the latter is applied to probe the generated terahertz waves. The terahertz polarizer P1 is mounted on the convergence position of vertical axis paraboloid mirror and P2 is installed in the middle of the third and the last. To guarantee the accuracy of terahertz polarization measurement, the grid of P2 keep consistent with the orientation of external magnetic field and P1 is used to adjusted to ±45° with respect to P2. After two polarizers, the terahertz waves are detected with electro-optic sampling (EOS) method. After being combined the THz waves are combined by a pellicle, the probe pulse is focused on a 2 mm thick ZnTe crystal, through a quarter-wave plate, a Wollaston prism, and collected by a pair of photodiodes.

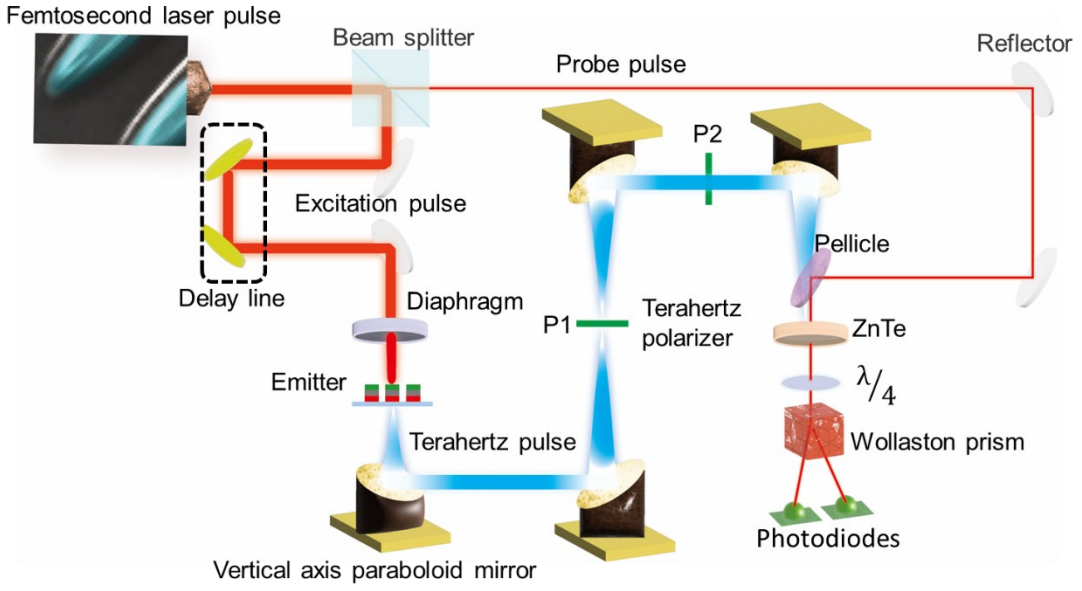

Fig. S2. The measurement equipment of the polarization-resolved terahertz time domain spectroscopy

system. Two terahertz polarizers (P1 and P2) are crucial to detect terahertz polarization waves.

S3 The change corresponding to azimuth angle in different stripes arrays where have no or strong current flow induced by the built-in electric field E_i.

In order to identify the influence from built-in electric fields on the terahertz waveforms with varying azimuth angles, the terahertz time domain spectroscopy $\boldsymbol{E_x}$ (parallel to magnetization) and $\boldsymbol{E_y}$ (normal to magnetization) from D1 and D7 are compared in Fig. S3.

Built-in electric fields play a remarkable role in the x direction. As Fig. S3(a) shown, $\boldsymbol{E_x}$ from D1 has no obvious change in amplitude value and time shift. Distinctly, in Fig. S3(b), the maximum value of $\boldsymbol{E_x}$ from D7 is twice lager than the minimum value accompanied by apparent time shift. The impact on $\boldsymbol{E_y}$ is illustrated in Fig. S3(c)-(d). On the y direction, D1 has no ability to emit terahertz waves. However, the amplitude value of D7 under the control of the built-in electric field has obvious fluctuations with the rotation of azimuth angle and phase reversal happens after 90°.

The error of the experimental results may come from the process of devices, the noise of the measurement setup and the rotation error of the angle turntable, all errors are within acceptable range.

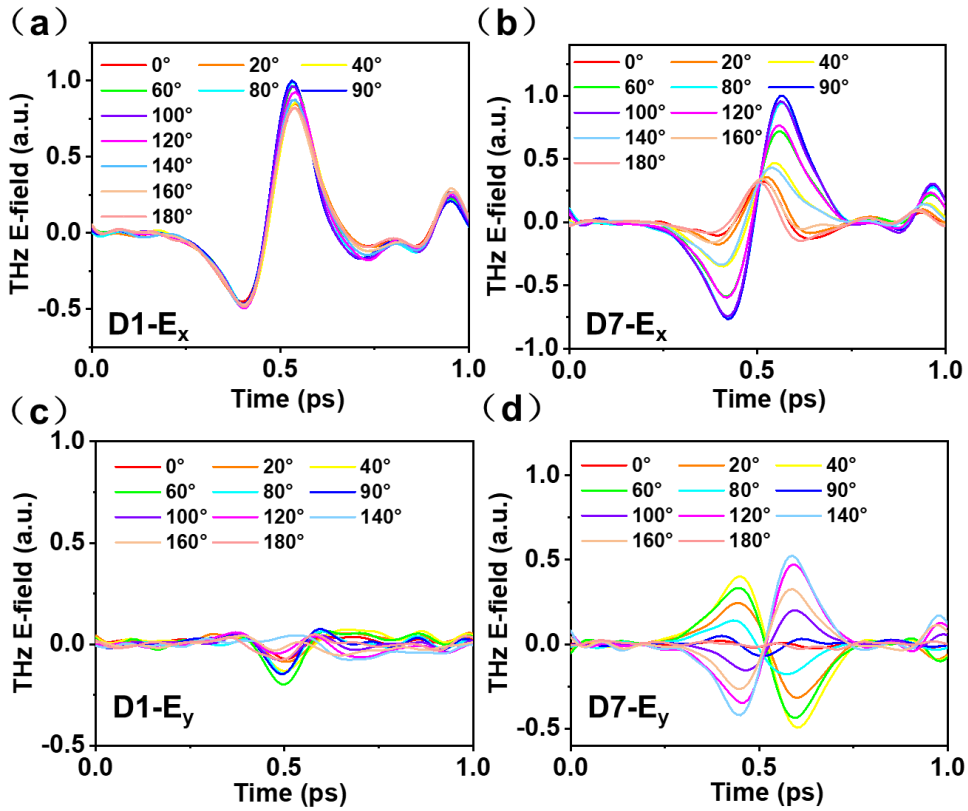

Fig. S3. Modulation of terahertz spectrum in different patterns. **(a)** Terahertz waveform of E_x under different azimuth angles in D1. **(b)** Terahertz waveforms of E_x under different azimuth angles in D7. **(c)** Terahertz waveforms of E_y under different azimuth angles in D1. **(d)** Terahertz waveforms of E_y under different azimuth angles in D7.

S4 The calculation of the built-in electric field E_i and the gap electric field E_s

As Fig. S4A shown, any positive charge staying at an edge (the position is set as point P) will be attracted by any negative charge on the other edges. Set the amount of charge per unit length on the edge be Q_i, the electric field strength excited by charges on the length dl is

$$\mathrm{d}E_i = \frac{Q_i dl}{4\pi\varepsilon_0 {r_1}^3}\overrightarrow{\boldsymbol{r_1}}, \tag{S1}$$

$$\mathrm{d}E_s = \frac{Q_i dl}{4\pi\varepsilon_0 {r_2}^3}\overrightarrow{\boldsymbol{r_2}}, \tag{S2}$$

where $\overrightarrow{r_1}$ and $\overrightarrow{r_2}$ are vectors from dl to point P in $\boldsymbol{E_i}$ and $\boldsymbol{E_s}$.

In the built-in electric field, the distance from any electron on the edge to the foot point O_1 is l_1, and the distance between the electron and P is $r_1=\sqrt{w^2+l_1^2}$. The angle between $\boldsymbol{dE_i}$ and the y axis is θ, the components of $\boldsymbol{dE_i}$ along the x axis and the y axis are

$$\mathrm{d}E_{ix} = \mathrm{d}E_i sin\theta, \tag{S3}$$

$$\mathrm{d}E_{iy} = \mathrm{d}E_i cos\theta, \tag{S4}$$

As displayed in Fig. S4(a),

$$\mathrm{d}l = \mathrm{w}csc^2\theta \mathrm{d}\theta, \tag{S5}$$

so,

$$\mathrm{d}E_{ix} = \frac{Q_i sin\theta d\theta}{4\pi\varepsilon_0 w}, \tag{S6}$$

$$\mathrm{d}E_{iy} = \frac{Q_i cos\theta d\theta}{4\pi\varepsilon_0 w}, \tag{S7}$$

We integrate the above equation to calculate built-in electric fields formed by the interaction between all charges on the boundary and any charge on the other side, thus:

$$E_{ix} = \int_{\theta_2}^{arcsin\frac{l}{\sqrt{l^2+w^2}}+\theta_1} \frac{1}{4\pi\varepsilon_0}\frac{Q_i}{w} sin\theta d\theta, \tag{S8}$$

$$E_{iy} = \int_{\theta_2}^{arcsin\frac{l}{\sqrt{l^2+w^2}}+\theta_1} \frac{1}{4\pi\varepsilon_0}\frac{Q_i}{w} cos\theta d\theta, \tag{S9}$$

As Fig. S4(b) illustrates, the sum of electric field component in the y direction is zero due to the symmetry of charge distribution, so only the electric field component in the x axis is concerned here.

Similarly, it can be concluded that in the gap electric field,

$$E_s = \int_{\alpha_2}^{arcsin\frac{l}{\sqrt{l^2+w^2}}+\alpha_1} \frac{1}{4\pi\varepsilon_0}\frac{Q_i}{w} sin\alpha d\alpha, \tag{S10}$$

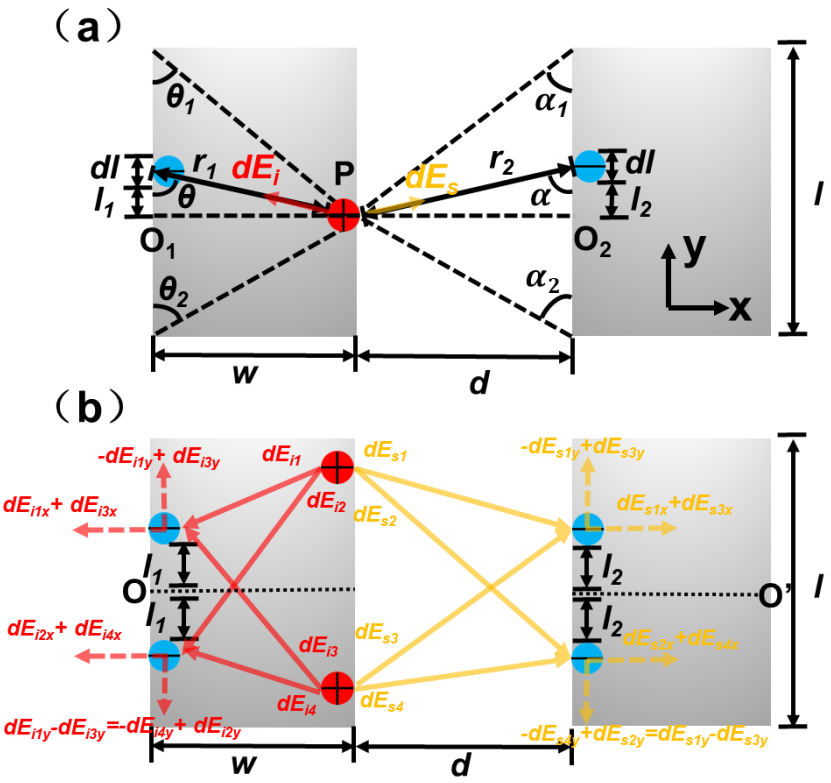

Fig. S4. The diagram of electric fields from charges on boundaries. **(a)** The electric field $\boldsymbol{E}_i$ and $\boldsymbol{E}_s$ are generated between any charges on adjacent edges of stripes. **(b)** The electric field between two opposite charges on both edges can be divided into the x and y direction. There always exists a pair of charges with opposite electric fields in the y-direction on the same side, unless $d\boldsymbol{E}_i$=$d\boldsymbol{E}_{ix}$. Therefore, the vector sum of all electrons in the y-direction is always 0.

S5 The working mechanism of antennas of the patterned terahertz emitters

The generation of photocurrent $\boldsymbol{j}_c$ originates from positive and negative charges flow in opposite directions, which can be regarded as dipole antennas induced by charges oscillation. According to the working principle of antennas, the length of charge oscillates path is crucial to the transmission performance of antennas. When the antenna size is less than one quarter of the transmission wavelength, the antenna exhibits

properties of capacitance, whereas antennas exhibit inductance when their size is greater than one quarter of the transmission wavelength[77,78]. The impedance modulus is

$$|X_c| = \sqrt{(R^2 + \frac{1}{(2\pi fC)^2})}, \tag{S11}$$

$$|X_L| = \sqrt{(R^2 + (2\pi fL)^2)}, \tag{S12}$$

where R is the resistance of a stripe, f is the frequency point, C is the equivalent capacitance and L is the equivalent reactance. Capacitive or inductive properties will affect the actual operating frequency range and center frequency of antennas.

The working frequency f_0 is the center frequency of antennas without these effects, which can be gotten by using Eqs. (S13):

$$f_0 = \frac{c}{z}, \tag{S13}$$

where c is the velocity of light, z is the path length of charge oscillation. f_0 of D1-D7 at 0° and 90° are shown in Fig. S5(c). The effective modulation frequency of stripes is between 0.4 THz~1 THz which is the 3dB band width of terahertz wave obtained from the homogeneous thin film W/CoFeB/Pt.

The frequency range of radiated terahertz waves includes the working frequencies of D1-D3. The highest transmission efficiency can be got at the corresponding frequency point, while the rest will experience frequency dependent transmission losses due to capacitance or inductance properties. Therefore, center frequencies f_c of D1-D3 vary greatly and are all similar to their work frequencies. As for D4, the working frequency f_0 is close to the center frequency 0.833 THz of terahertz waves emitted from W/CoFeB/Pt thin films. Therefore, its center frequency f_c is also located nearby.

Influenced by capacitance effect, the working frequencies of D5-D7 are outside the 3dB bandwidth (0.4 THz-1 THz), so terahertz waves emitted attenuates throughout the entire frequency range with decreasing frequency. Within the range of less than 1.17 THz (the f_0 of D5), the reduction at any frequency point of D5-D7 is almost equal, which makes their positions of f_c be also close to 0.833 THz. The above mentioned is consistent with the experimental phenomenon described in Fig. 2(b). The information loss of D4-D7 in lower frequency (about 0-0.2 THz) takes root in exceeding the working bandwidth of antennas, and the sharp decrease of D1-D3 in higher frequency (1.2-1.5 THz) is the result of intense inductive reactance. As a result, the expand of full width at half maximum (FWHM) ΔF in Fig. 2(b) were caused.

When emitters rotate to 90°, owing to no gap electric field in the direction of $\boldsymbol{j}_c$, the length of antennas is always twice of l. The working frequencies of all samples are less than 0.4 THz; thus, all samples are affected by the inductance in 0.4~1 THz according to Eqs. (S12). Therefore, no noticeable shift in the positions of f_0 as Fig. 2(e) depicted. As for ΔF, the working frequency of D1 are around 0.265 THz and alleviate information loss with l increases. As a result, capacitive resistance in lower frequency range causes a climb in D1-D7.

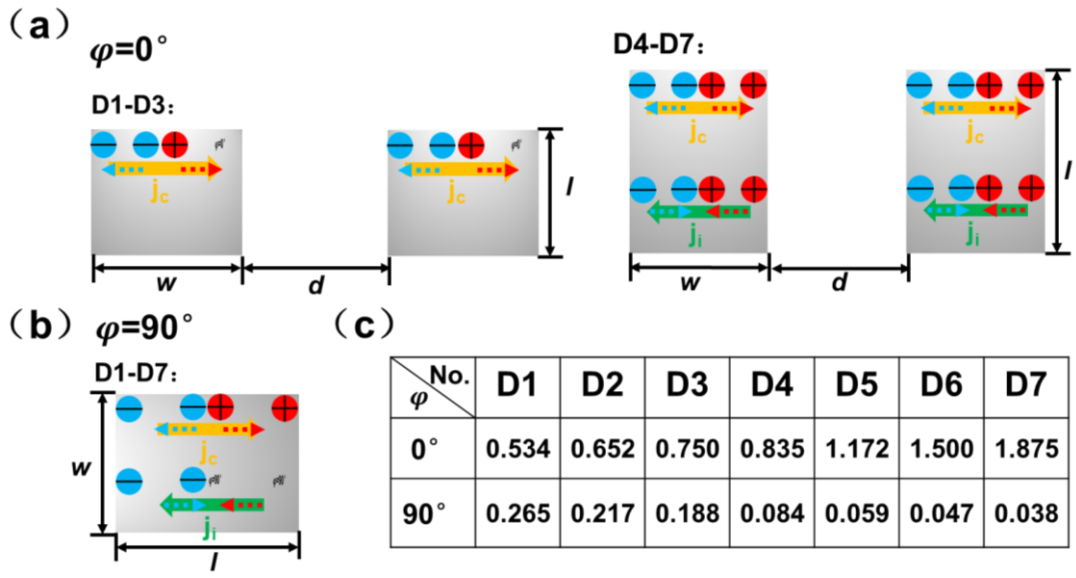

No. / φ	D1	D2	D3	D4	D5	D6	D7
0°	0.534	0.652	0.750	0.835	1.172	1.500	1.875
90°	0.265	0.217	0.188	0.084	0.059	0.047	0.038

Fig. S5. The antennas effect in patterned terahertz emitters. **(a)** When φ=0°, there is no backflow $\boldsymbol{j}_i$ in D1-D3, so the path of charge oscillation is equal to the distance traveled by $\boldsymbol{j}_c$. In D4-D7, photocurrent $\boldsymbol{j}_c$ and backflow $\boldsymbol{j}_i$ make the path of charge oscillation become 2l. **(b)** When φ=90°, charges oscillation inside D1-D7 also occurs in both the picosecond photocurrent $\boldsymbol{j}_c$ and backflow $\boldsymbol{j}_i$. **(c)** The working frequency f_0 (unit: THz) of D1-D7 at 0° and 90°.

S6 The polarization modulation results of relevant analysis

Rotating samples only changes the relative position of samples and the external magnetic field, thus the flow direction of the generated picosecond current $\boldsymbol{j}_c$ and the vector sum of the back flow $\boldsymbol{j}_i$ are vertical to $\boldsymbol{M}$. In order to simplify the model, the gap electric field are not drawn.

As Fig. S6(a) shown, when φ is 0°, charges at both edges attract each other and form a current $\boldsymbol{j}_a$ which is opposite to $\boldsymbol{j}_c$ due to the strength of the built-in electric field being greater than the strength of the gap electric field. Although there is no built-in electric field along the long side, to more intuitively demonstrate the rearrangement

of charges within the stripes during rotation, we assume that there is also a backflow along the long side, denoted by j_b. The macroscopic manifestation is a weakening on the terahertz amplitude with the increase of *l*/*w*. Similarly, when the azimuth angle reaches to 90°, as displayed in Fig. S6(c), owing to no gap electric field, charges at both edges also attract each other and form a backflow $\boldsymbol{j_i}$. According to Eqs. (1), $\boldsymbol{j_i}$ is proportional to $\boldsymbol{j_a}(w/l)^4$.

In other contexts, as unfolded in Fig. S6(b) and (d), electrons are distributed over two neighboring sides of a stripe. $\boldsymbol{j_c}$ can be decomposed into $\boldsymbol{j_{cp}}$ along *l* and $\boldsymbol{j_{cv}}$ along *w*. $\boldsymbol{j_i}$ is supposed to be handled in the same way. Note that the relevant component of $\boldsymbol{j_i}$ come from the accumulating charges, so $\boldsymbol{j_{iv}}$ and $\boldsymbol{j_{ip}}$ cannot be calculated directly by vector decomposition. During the rotating process, the back flow and charges distribution are deeply affected by the azimuth angle, so each current can be represented by $\boldsymbol{j_c}$, $\boldsymbol{j_a}$, $\boldsymbol{j_b}$ and corresponding azimuth angles.

As for 0°<φ<90°, each current meet:

$$j_{cv} = j_c cos\varphi, \tag{S14}$$

$$j_{cp} = j_c \sin\varphi, \tag{S15}$$

$$j_{iv} = j_a \cos\varphi - j_b \sin\varphi, \tag{S16}$$

$$j_{ip} = -j_a \sin\varphi + j_b \cos\varphi, \tag{S17}$$

As for 90°<φ<180°,

$$j_{cv} = -j_c cos\varphi, \tag{S18}$$

$$j_{cp} = j_c \sin\varphi, \tag{S19}$$

$$j_{iv} = j_a \cdot \cos\varphi - j_b \sin\varphi, \tag{S20}$$

$$j_{ip} = j_a \cdot \sin\varphi - j_b \cos\varphi, \tag{S21}$$

Due to detection terminal of THz-TDS towards x and y directions, each current along sides should be divided into x and y directions for polarization analysis. During rotating from 0° to 90°, current in the x direction is:

$$j_x = j_c - j_a \cos 2\varphi, \tag{S22}$$

Current in the y direction is:

$$j_y = j_b - j_a \sin 2\varphi, \tag{S23}$$

During rotating from 90° to 180°, current in the x direction is:

$$j_x = j_c - j_a \cos 2\varphi, \tag{S24}$$

Current in the y direction is:

$$j_y = -j_b + j_a \sin 2\varphi, \tag{S25}$$

The above formulas reveal that the amplitude variation of stripes with different aspect ratios during rotation and the reason for the change of handedness of polarization before and after 90°. As there is the analysis and discussion of the current distribution which induces the generation of terahertz polarization, the above only applies to D4-D7.

As regards D1-D3, charges on *l* steadily accumulate at the edge and will not form backflow as the result of the greater gap electric field compared to built-in electric field, thus j_a is 0, so there is no chirality variety in D1-D3.

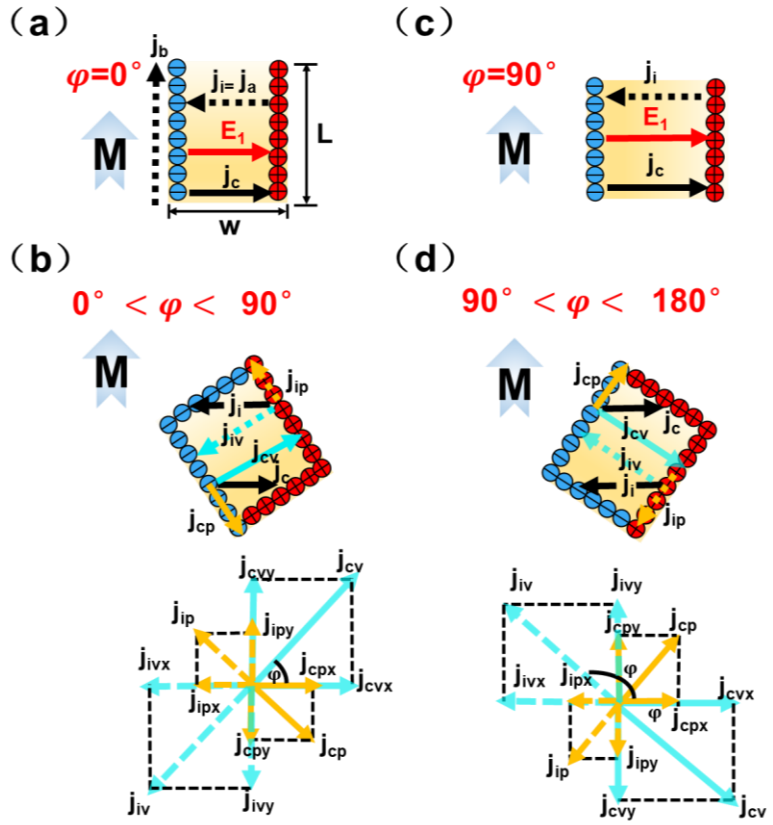

Fig. S6. Electrons and current distribution in x and y directions under all different azimuth angles.

S7 The derivation process of the phase difference in time domain

Time shift in a signal always brings about the appearance in phase transform[79]. Therefore, how to describe the dependency relationship between two random signals is the key element to acquire the phase difference[80]. Here, correlation function can make a contribution to obtain the delay of terahertz wave between x and y direction and we can get the corresponding phase difference through converting the delay to the angle[81,82].

The phase difference could be gotten by Eqs. (S26) -(S29):

$$R_{xx}(n) = \sum_{n=-\infty}^{+\infty} x(m)x(n-m), \tag{S26}$$

$$R_{yy}(n) = \sum_{n=-\infty}^{+\infty} y(m)y(n-m), \tag{S27}$$

$$R_{xy}(n) = \sum_{n=-\infty}^{+\infty} x(m)y(n-m), \tag{S28}$$

$$\Delta\beta = \cos^{-1}((R_{xy}(0)/(\sqrt{R_{xx}(0)R_{yy}(0)})), \quad \text{(S29)}$$

where $R_{xx}(n)$ and $R_{yy}(n)$ are autocorrelation function of terahertz in the x and y direction, and $R_{xy}(n)$ is the cross-correlation function of terahertz waves in the x and y direction. The symbol *n* represents discrete-time variable and *m* is the number of sampling periods between two random variables. We can get the value of phase difference in time domain when n=0.

S8 The photocurrents in a short excitation model

According to the mechanism of photocurrents generation, $\boldsymbol{j_c}$, $\boldsymbol{j_a}$ and $\boldsymbol{j_b}$ originate in the process of optical excitation transfers electrons from initial states into final states and the spatial shift of electron density distribution, which can be phenomenologically expressed as the form of injection currents and shift currents. For the short enough excitation, this process leads to a step-like charge displacement $\Delta x_{sh}\Theta(t)$ whose temporal derivative is proportional to the injection current $\boldsymbol{j_{inj}}$ and the shift current $\boldsymbol{j_{sh}}$[84-87]:

$$j_{inj} \propto \frac{\partial}{\partial t}\left(\Delta z_{inj}\Theta(t)e^{-\frac{t}{\tau_{inj}}}\right) * I_p(t), \quad \text{(S30)}$$

$$j_{sh} \propto \frac{\partial}{\partial t}\left(\Delta x_{sh}\Theta(t)e^{-\frac{t}{\tau_{sh}}}\right) * I_p(t), \quad \text{(S31)}$$

where $\Theta(t)$ is the unit step function, Δz_{inj} is the thickness of the emitting sheet, the exponential decay with time constant τ_{inj} and τ_{sh} represent relax processes, and $I_p(t)$ is the pump intensity envelop which is normalized to unity. The convolution (denoted by *) with the pump intensity envelope $I_p(t)$ accounts for the shape of the pump pulse, resulting in a current with the typical temporal shape. In addition, as Fig. S7(a) shown,

we fit Eqs. (S30) -(S31) to $\boldsymbol{j_c}$ yields excellent agreement for a pump duration of 35 fs, repetition rate of 1000 KHz, τ_{inj} is 400fs and τ_{sh} is 37fs. As for D7, when τ_{sh} is 65fs, as Fig. S7(b) displayed, the fitting curves can also meet the measured $\boldsymbol{j_a}$ and $\boldsymbol{j_b}$. The increase in relaxation time is due to the lower average velocity of back flow than $\boldsymbol{j_c}$. According to Eqs. (1), changes in l and w would affect the strength of $\boldsymbol{E_i}$, which has impact on amplitude of $\boldsymbol{j_a}$ and $\boldsymbol{j_b}$. When we introduce the rate of change in l or w into the scale factor of Eqs. (S30) -(S31), the profiles of $\boldsymbol{j_a}$ and $\boldsymbol{j_b}$ at various aspect ratio can be obtained. For example, as Fig. S7(c) shown, the fitting of backflow of D4 is consistent with the measured curve.

By substituting Eqs. (S30) into Eqs. (S22) -(S23), currents in the x and y directions $\boldsymbol{j_x}$ and $\boldsymbol{j_y}$ can be obtained, which satisfies

$$\nabla^2 \boldsymbol{E} + \omega^2 \mu_0 \varepsilon \boldsymbol{E} = \mu_0 i \omega j, \tag{S32}$$

where ω is the angular frequency, ε is the dielectric constant, μ_0 is the vacuum permeability and $\boldsymbol{E}$ represents the electric field of terahertz waves. Thus, $\boldsymbol{E_{THz,x}}$ and $\boldsymbol{E_{THz,y}}$ are proportional to $\boldsymbol{j_x}$ and $\boldsymbol{j_y}$. The fits of the change trend of THz electric field peak with aspect ratio as a function of φ, $\boldsymbol{j_a}$ and $\boldsymbol{j_b}$ using Eqs. (S22) -(S23) (Fig. 2(a), Fig. 2(d), Fig. 3(c)-(e)) are highly consistent with the experimental data. Eqs. (S22) -(S23) can also be used to calculate the phase difference temporally with Eqs. (S26) -(S29), as shown in Fig. 3(b), the fits of $\Delta\beta$ can match results obtained in the experiments.

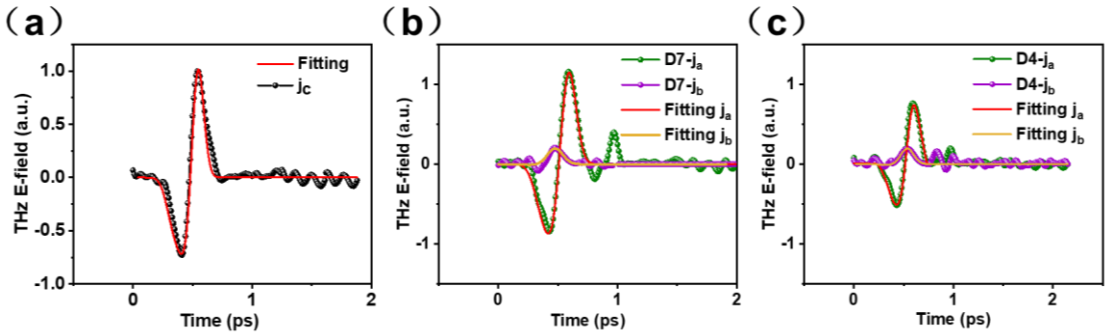

Fig. S7. The measured THz waveforms and fittings. **(a)** j_c, **(b)** j_a and j_b of D7 and **(c)** j_a and j_b of D4.

S9 The Stokes parameters for calculating ellipticity in time and frequency domain

Here, we define E_x, E_y as the modulus of the Fourier transformed spectra in the x and y directions, and the Stokes parameters are represented as $(S_0, S_1, S_2, S_3)^{\mathrm{T}}$. The Stokes matrix in time domain can be represented as

$$\mathrm{S}=\begin{bmatrix}S_0\\S_1\\S_2\\S_3\end{bmatrix}=\begin{bmatrix}E_x^2+E_y^2\\E_x^2-E_y^2\\2E_xE_y\cos\Delta\beta\\2E_xE_y\sin\Delta\beta\end{bmatrix}, \tag{S33}$$

And for frequency domain,

$$\mathrm{S}=\begin{bmatrix}S_0\\S_1\\S_2\\S_3\end{bmatrix}=\begin{bmatrix}E_x^2+E_y^2\\E_x^2-E_y^2\\2Re(E_xE_y^*)\\-2\cdot\mathrm{Im}\,(E_xE_y^*)\end{bmatrix}, \tag{S34}$$

Ellipticity in both situations can be expressed by:

$$e=\tan\left(\arcsin\left(-\frac{S_3}{S_0}\right)\cdot 0.5\right), \tag{S35}$$

which reminds that the ellipticity distribution in the fully frequency is one of regulation behavior indexes of D7. The ellipticity of e is positive for the left-handed wave and negative for the right-handed wave. In particular, e=1 stands for an ideal circular polarization wave and e=0 represents a linear polarization wave.

S10 The polarization regulation results of other devices

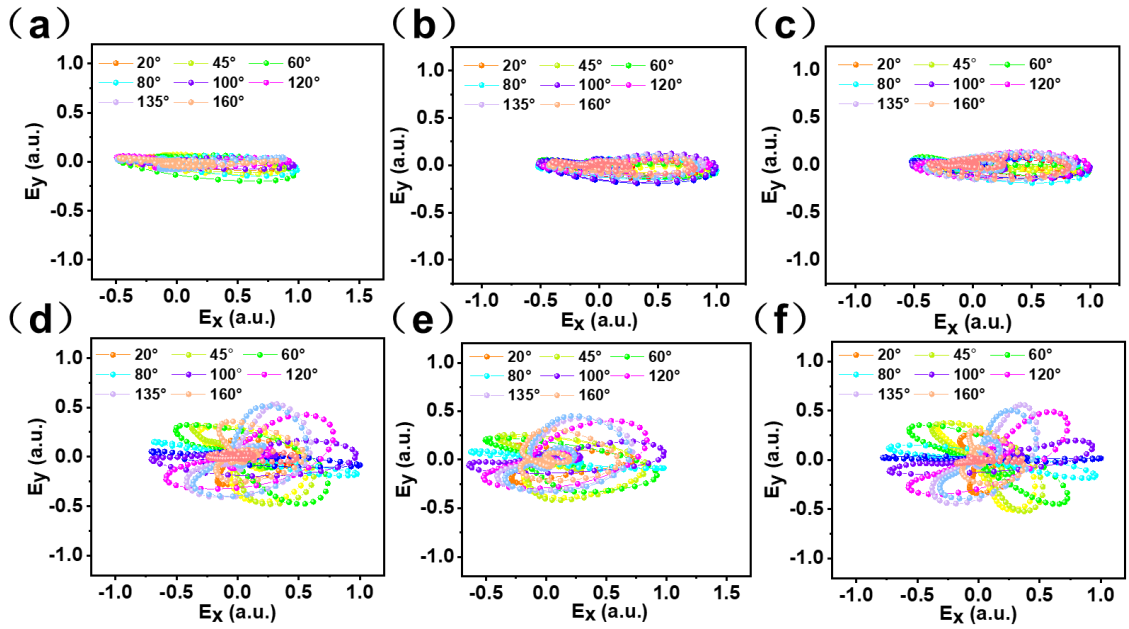

Fig. S8. Polarization regulation with azimuth angles of D2-D6. **(a)** D2, **(b)** D3, **(c)** D4, **(d)** D5 and **(e)** D6.

S11 Magnetic properties of all samples at 0° and 90°

The magnetic properties of the spintronic-metasurface samples are characterized using a MOKE setup. As shown in Fig. S9, stripes with different aspect ratio exhibit similar hysteresis loops with a coercive of ~30 mT whether at 0° or 90°. It is noted worthy that coercive fields for these samples with 0° and 90°are nearly consistent with each other, which indicates that the magnetic shape can be negligible in this experiment and the difference in terahertz emission is also independent of magnetic anisotropy.

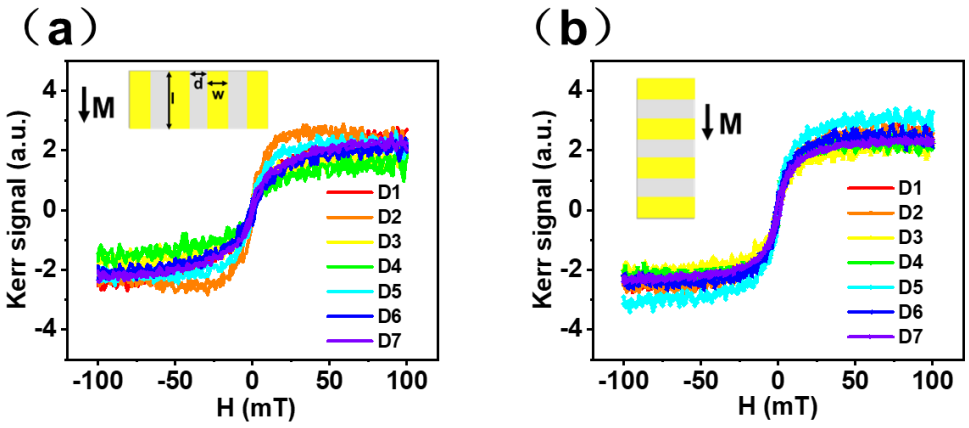

Fig. S9. The hysteresis loops of all samples at 0° **(a)** or 90° **(b)** using the MOKE setup.

S12 Material and heterojunction structure selection

Based on inverse spin Hall effect (ISHE), the common magnetic materials mainly include Fe,Co,Ni, and their binary alloys. Previous work has indicated that Pt, W and Bi_2Te_3 are the best choices for non-magnetic materials. Here, we compare the emission performance of serveal heterojunctions in both time domain and frequency domain. As shown in Fig. S10 (a), W/CoFeB/Pt exhibits the optimal performance under the fixed pump power. These heterojunctions cover approximate bandwidth ~2.5 THz in Fig. S10 (b). Therefore, W/CoFeB/Pt is opted in this work.

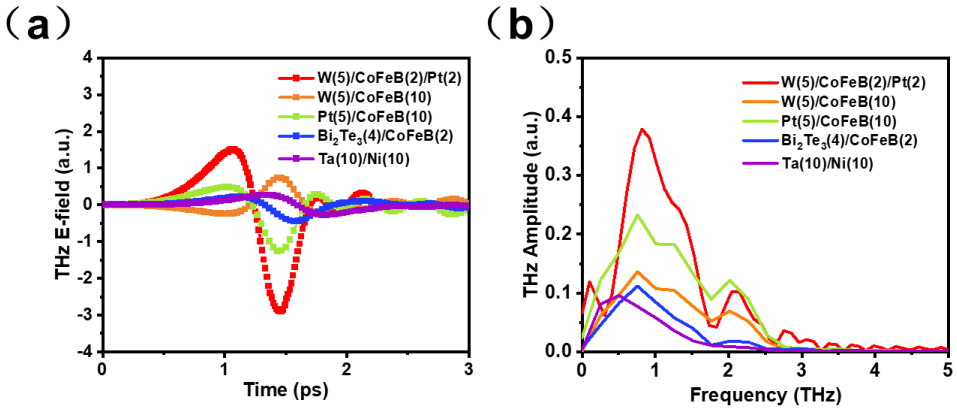

Fig. S10. Comparison of THz emission amplitude **(a)** and bandwidth **(b)** of different heterojunctions.

S13 the impact of magnetic field intensity on the emission

Here, we fixed D7 at 20° and the magnetic field is fixed in the y direction. The magnetic strength was adjusted by changing the number of static magnets. As shown in Fig. S11(a) and (b), the increase in magnetic field strength did not significantly increase the amplitude. The chirality modulation effect is also remains similar in Fig. S11(c). The characteristics that remain independent of magnetic field strength are attributed to the device's small coercive field about 30 mT, which reveals that our device can still maintain stable performance in a varying magnetized environment.

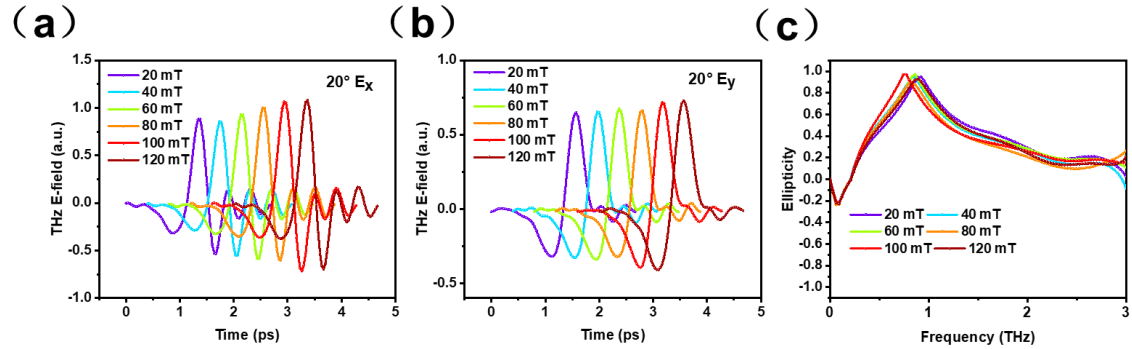

Fig. S11. (a) –(b) The amplitude in the x and y direction under different strength magnetic fields. **(c)** The ellipticity modulation under different strength magnetic fields.